JTE HCMUTE
ISSN: 2615-9740

JOURNAL OF TECHNICAL EDUCATION SCIENCE
Ho Chi Minh City University of Technology and Education
Website: https://jte.edu.vn
Email: jte@hcmute.edu.vn

Fabrication of Heterostructure g-C_3N_4/BiOCl for Degradation of Rhodamine B Dye Under Visible Light

Van-Tai Nguyen, Thu-Thao Tran-Thi, Thanh-Truc Pham*
Ho Chi Minh City University of Technology and Education, Vietnam

*Corresponding author. *Email*: trucpt@hcmute.edu.vn

ARTICLE INFO

Received: 07/08/2024
Revised: 18/09/2024
Accepted: 28/10/2024
Published: 28/05/2025

KEYWORDS

Bismuth oxychloride;
Graphitic carbon nitride;
Heterostructure;
Photocatalyst;
Visible light.

ABSTRACT

In this paper, we combined bismuth oxychloride (BiOCl) and graphitic carbon nitride (g-C_3N_4) to in g-C_3N_4/BiOCl heterostructure photocatalysts for the rejection of organic contaminants in wastewater. At first, the bulk g-C_3N_4 was delaminated into a few-layer g-C_3N_4 suspension in water. Afterward, the photocatalysts were blended via the sol-gel method with the combination of the g-C_3N_4 suspension at numerous g-C_3N_4/BiOCl ratios. The methodology, morphology, optical properties, and photocatalytic activity of the g-C_3N_4/BiOCl series were discussed in detail. The combination of the two-dimensional plate structure of g-C_3N_4 and BiOCl was examined through scanning electron microscopy (SEM), surface area (BET), X-ray diffraction (XRD), Fourier transform infrared spectroscopy (FTIR), and UV-Vis diffuse reflectance spectroscopy (DRS). Since BiOCl and g-C_3N_4 are both semiconductors, it is expected that BiOCl sheets will be well dispersed on the surface layers of g-C_3N_4 to form a heterostructure with the heterogeneous charge transfer model, providing significant removal of Rhodamine B (RhB) dye under visible light. Such a combination has the potential to overcome the disadvantages of pristine BiOCl and g-C_3N_4 improve the photocatalytic activity, and shorten the wastewater treatment time.

Doi: https://doi.org/10.54644/jte.2025.1636

1. Introduction

Nowadays, the development of modern industries leads to numerous serious environmental pollution issues such as soil pollution, air pollution, water pollution, etc. Scientists have focused on researching high-application materials in the environmental field, particularly photocatalytic materials for treating organic waste in water [1], [2], [3]. The photocatalytic process utilizes natural sunlight radiation, which can be easily and widely used on large-scale fields. Rhodamine B (RhB), a common industrial dye, is a major cause of water pollution and toxic to organisms, potentially causing cancer with prolonged exposure [4], [5].

Bismuth oxychloride (BiOCl) is a p-type semiconductor with stability, superior photocatalytic efficiency, an indirect bandgap transition, non-toxicity, and a layered crystal structure. Which are bonded through an internal electrostatic field that can improve the division and transport of electron (e^-) and hole (h^+) pairs [6]. However, BiOCl has a relatively large bandgap (3.2 – 3.6 eV), so it can only be excited by UV light [7]. Various studies have been executed to improve the bandgap and quantum efficiency of BiOCl, such as adjusting the heterostructure to enhance photocatalytic activity [8]-[11]. Graphitic carbon nitride (g-C_3N_4) is a polymer semiconductor with a small bandgap and good light response, but it has a small surface area and reduced light absorption rate at wavelengths greater than 460 nm [12]. The swift recombination of electrons and holes is a problem that needs to be resolved for g-C_3N_4. By combining materials (Ag, RGO) with good electrical conductivity of semiconductors (ZnO, TiO_2), the composite material shows enhanced photocatalytic efficiency due to the effective separation of e^- and h^+ [13]-[18]. Particularly, the development of heterostructure materials is being promoted to take advantage of the benefits, improve limitations, and thus maximize the photochemical efficiency of the materials.

The heterostructure of g-C_3N_4 and BiOCl efficiently separate and transfer charges, reducing the recombination probability of carrier charge, to improve photocatalytic efficiency. Many studies have shown that incoporating g-C_3N_4 and BiOCl could lead to higher photocatalytic efficiency [7], [19]-[26]. However, most of the studies are focused on the bulk g-C_3N_4 and tested with high power lamp. In this paper, the g-C_3N_4/BiOCl heterostructure was successfully synthesized from exfoliated g-C_3N_4 and BiOCl by sol-gel method. The results narrow the quantum transition energy of BiOCl to enhance catalytic efficiency under visible light, with the goal of degrading RhB in industrial wastewater under low power LED lamp.

2. Materials and Experimental

2.1. Materials and Chemicals

Chemicals were utilized directly without further purification. Urea, sulfuric acid (98%), acetic acid (99%), ethanol (99.9%), ethylene glycol (EG), isopropanol (IPA), potassium dichromate ($K_2Cr_2O_7$), ethylenediaminetetraacetic acid (EDTA-2Na), p-benzoquinone (BQ) were obtained from Xilong Chemicals (China). Thiourea (TU), bismuth (III) nitrate pentahydrate ($Bi(NO_3)_3{\cdot}5H_2O$), potassium chloride (KCl), and rhodamine B (RhB) were obtained from Sigma (Merck).

2.2. Synthesis of g-C_3N_4/BiOCl Heterostructure

2.2.1. Synthesis of Water-Dispersible g-C_3N_4

g-C_3N_4 was synthesized through two processes: (i) Urea was used as a precursor in a thermal polycondensation process to create bulk g-C_3N_4 (CNb), and (ii) The CNb product was oxidized using an oxidizing mixture of H_2SO_4 and $K_2Cr_2O_7$. Specifically, urea was heated to 550°C for 5 hours at a heating rate of 3°C/min. After completing the thermal treatment, the CNb product was delaminated by oxidation. 4 g of $K_2Cr_2O_7$ was slowly added to 20 ml of H_2SO_4 (98%) and stirred until the solution turned brown, then 0.2 g of CNb was added and stirred for 4 hours without heating. The reaction blend was quickly poured into 200 ml of DI water and allowed to cool to room temperature, followed by multiple washes until pH = 7. The resulting white solid was dispersed in DI water by sonication for 2 hours. Finally, the solution was centrifuged at 3000 rpm for 5 minutes to eliminate undelaminated g-C_3N_4. The product was fully water-dispersible g-C_3N_4 with a concentration of 5 mg/ml, denoted as CNs.

2.2.2. Synthesis of BiOCl

The synthesis of BiOCl was carried out as follows: 0.005 mol of $Bi(NO_3)_3{\cdot}5H_2O$ was dissolved in 50 ml of an EG-H_2O mixture (1:1). Then, 0.5 mol of TU was added to the solution, and upon observing the formation of a white suspension, 0.005 mol of KCl was added, and the stirring speed was increased. While stirring, 50 ml of 2% acetic acid solution was slowly added and stirred continuously for 1 hour. The resulting solid was filtered and cleaned with DI water and ethanol. Finally, the washed solid was dried to a constant weight at 60°C for 12 hours.

2.2.3. Synthesis of g-C_3N_4/BiOCl Heterostructure

Similar to the BiOCl synthesis procedure, after adding TU to the system, x grams of CNs (where x is the weight percentage of CNs) were added. The subsequent steps remained unchanged. The resulting g-C_3N_4/BiOCl heterostructure products were denoted as BCN-x, with x being 2%, 4%, 6%, and 8% by weight of g-C_3N_4.

2.3. Characterization

The crystal structure of the samples was inspected using X-ray diffraction (XRD, Empyrean – PANalytical) with Cu-Kα radiation (λ = 1.54 Å). The morphology and microstructure of the samples were analyzed using field emission scanning electron microscopy (FE-SEM, Regulus 8100, Hitachi). Specific surface area and pore size were measured using Brunauer–Emmett–Teller (BET) surface area and pore size analyzer (TriStar II Plus 3.03). Functional groups were determined using Fourier-transform infrared spectroscopy (FT-IR, Nicolet 6700, Thermo). Bandgap widths were analyzed using UV diffuse reflectance spectroscopy (DRS, V-570 UV/VIS, Jasco). Light absorption efficiency was evaluated using UV-Vis absorption spectroscopy (CRF - V-730, Jasco).

2.4. Photocatalytic Experiments

Photocatalytic activity was assessed by RhB degradation in water using visible light. 25 mg of BCN-x was added to 100 ml of RhB solution (10 ppm). The solution was then subjected to adsorption equilibrium for 30 minutes. After adsorption, the solution was irradiated for 60 minutes using a 50W-220V white LED lamp. The degradation of RhB was determined by calculating the reduction in concentration at a wavelength of 553 nm at specific time intervals using UV-Vis absorption spectroscopy (CRF - V-730, Jasco).

3. Results and Discussion

3.1. Characterization

XRD method was employed to analyze the crystal phase structure of the synthesized samples. **Figure 1 (a)** shows the XRD spectra of BiOCl, CNb, and BCN-6 samples. For CNb, the strongest and most distinct diffraction peak at 27.5° corresponds to the (002) plane, characteristic of the stacking of single layers with its aromatic ring structure. The weaker peak at 12.7° is the (100) plane of CNb, caused by the in-plane linkage of tri-s-triazine units. In bulk form, CNb consists of multiple stacked single layers, making the (002) plane diffraction peak the strongest [27]. For pure BiOCl, all diffraction peaks match those of tetragonal-phase BiOCl reported in the card ICDD 01-085-0861 [27], [28], [29]. The 2θ diffraction peaks with values of 11.84°, 24.07°, 25.91°, 32.61°, 33.47°, 34.81°, 36.52°, 40.96°, 46.76°, 48.44°, 49.73°, 54.25°, 58.71°, 60.65°, 68.30°, 75.12°, and 77.80° correspond to the planes (001), (002), (101), (110), (102), (111), (003), (112), (200), (201), (113), (211), (212), (114), (220), (214), and (310) [27], [28]. For CNb and BiOCl materials, the characteristic peaks for both phases match the data in previous reports [20], [27], [28], with no other peaks detected, indicating high purity and no formation of by-products. For the BCN-6 composite material, the characteristic peaks of BiOCl were observed in the material, showing the existence and structural maintenance of BiOCl in the composite. However, the peaks of CNb did not appear in the composite material, possibly due to the relatively low CNs content and delaminated structure caused by strong oxidation, making detection by XRD difficult.

Furthermore, when focusing on the (101), (110), and (102) peaks **(Figure 1b)**, no peak shift occurred in the BCN-6 sample compared to BiOCl, which indicates the preservation of the BiOCl phase structure inside the BCN-6 sample and that no phase change of BiOCl occurred during the synthesis process. Based on equation (1), the crystal sizes of BiOCl and BCN-6 at the (101) peak are 16.41 nm and 16.78 nm, respectively. These sizes are almost unchanged, however, BCN-6 appears to be slightly larger than BiOCl. The formula for calculating crystal size is based on the Scherrer equation:

$$D = \frac{k \times \lambda}{\beta \times cos(\theta)} \quad (1)$$

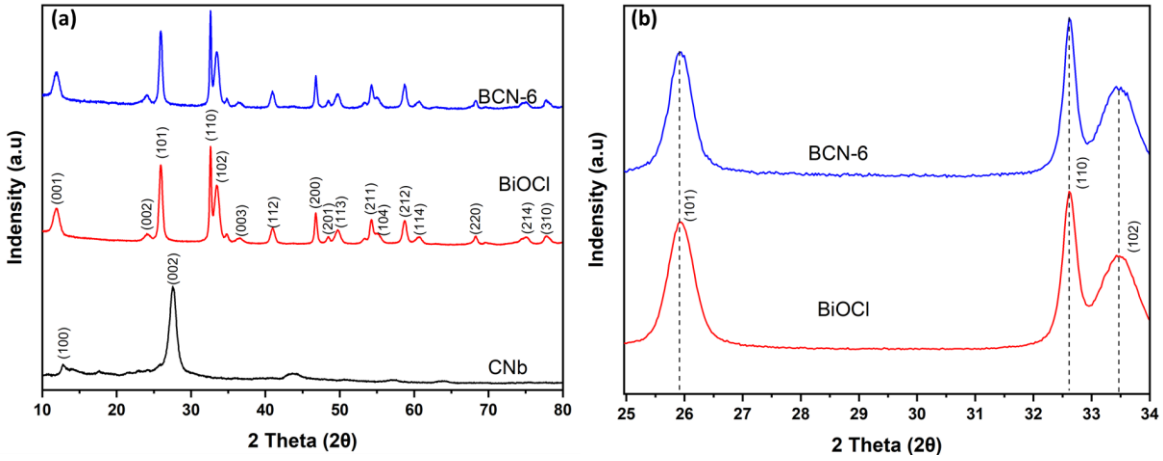

Figure 1. *(a) XRD diffraction patterns of BiOCl, CN, and BCN-6 samples, (b) Enlargement of the (101), (110), and (102) peaks of BiOCl and BCN-6*

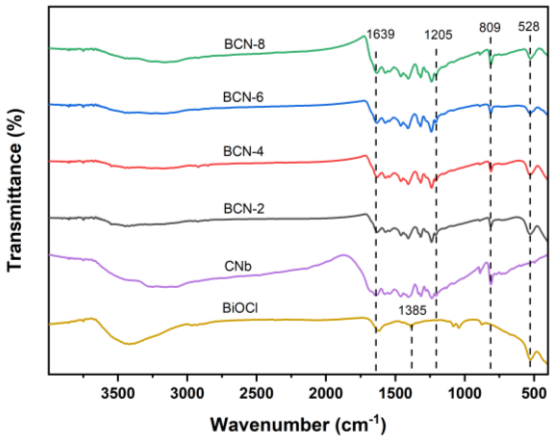

Figure 2. *FT-IR spectra of BCN-x composite samples, BiOCl, and CNb*

Where λ is the X-ray wavelength (nm), k is the shape factor (0.9), θ is the diffraction angle (rad), β is the full width and half maximum (rad) and D is the crystal size (nm).

In **Figure 2**, the FT-IR spectra of CNb show peaks appearing at 809 cm^{-1}, characteristic of the vibrations of tri-s-triazine rings, while the peak at 1639 cm^{-1} relates to the stretching vibration of C=N bonds, and peaks ranging from 1205 to 1639 cm^{-1} are associated with the stretching of aromatic C-N bonds [20], [30]. Regarding the FT-IR spectrum of BiOCl, the absorption peak at 528 cm^{-1} is attributed to the stretching vibration of Bi-O in the tetragonal phase of BiOCl crystals [20]. Another peak at 1385 cm^{-1} are attributed to the asymmetric stretching vibrations of Bi-Cl bonds [31]. The peak at 1623 cm^{-1} corresponds to the vibrations of O-H bonds in water molecules, possibly from moisture in the air [32], overlapping with the peak at 1639 cm^{-1} of CNb, indicating a slight shift between the peaks of BiOCl compared to CNb and the BCN-x samples. All composite samples show the presence of characteristic peaks of BiOCl and CNb, demonstrating that the composite maintains the basic structure of CNs and BiOCl after incorporation of CNs.

The morphology and size of the particle are determined by SEM. **Figure 3a** shows the SEM image of pure BiOCl with a flower-like structure about 0.7 μm in size consisting of many BiOCl plates aggregated together, each BiOCl plate having an average thickness of about 15 nm and a size of about 100 nm. Meanwhile, CNb consists of multiple stacked layers with uneven sizes **(Figure 3b)**. After undergoing oxidation with $K_2Cr_2O_7$ and H_2SO_4, the structure becomes more porous, and the size of each layer becomes smaller and thinner **(Figure 3c)**. A heterostructure forms when CNs are added to BiOCl. During this process, the bismuth precursor decomposes in water to form Bi^{3+} ions, which then combine with the -OH group in EG to form the $Bi(OCH_2CH_2OH)^{2+}$ complex. After adding TU, TU binds to this complex to form a new complex $Bi(OCH_2CH_2OH)(Tu)^{2+}$ because the lone pairs of electrons on the N and S atoms in the TU molecule can bind to Bi ions [9]. In the tri-s-triazine ring structure, the N atoms are more electronegative than the C atoms, so the active sites of the N atoms will have a more negative charge. As a result, the positively charged $Bi(OCH_2CH_2OH)(Tu)^{2+}$ complexes can be electrostatically adsorbed onto the active sites of the N atoms [14]. When Cl^- ions are present, they gradually replace

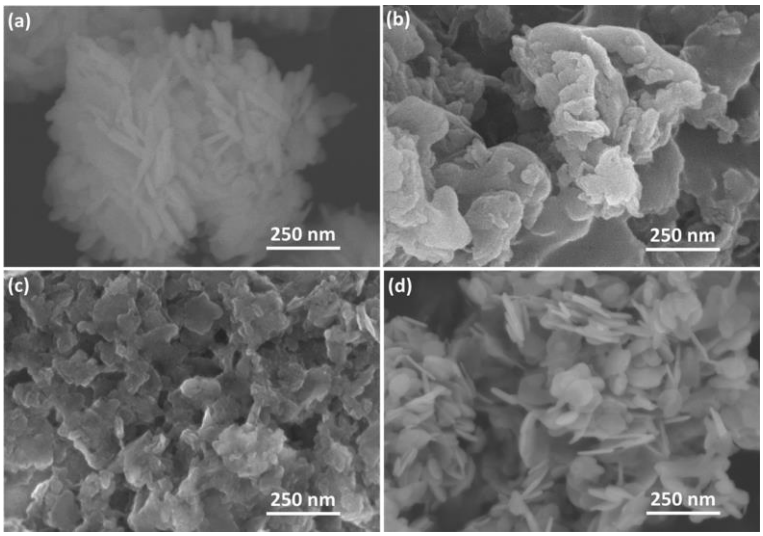

Figure 3. *SEM images of (a) pristine BiOCl, (b) CNb, (c) CNs and (d) BCN-6.*

TU, and then BiOCl crystal nuclei can grow into a 2D sheet-like structure on the surface of CNs. During the growth process, because Bi^{3+} ions adhere to the surface of CNs before developing into BiOCl sheets, **Figure 3d** shows BiOCl sheets adhering to the surface of CNs, which is different from the structure of pure BiOCl.

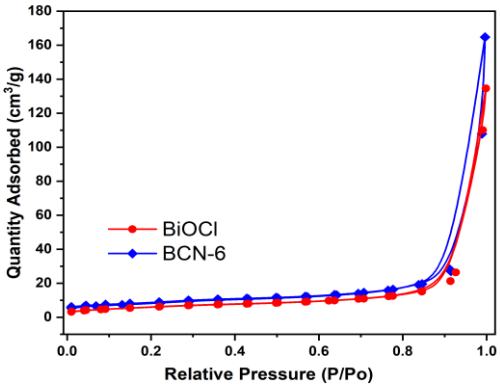

Figure 4. *N_2 adsorption–desorption isotherms of pure BiOCl, and BCN-6*

One factor affecting the pollutant degradation efficiency is the specific surface area of the catalyst. A catalyst with a significant specific surface area increases the ability to adsorb pollutants and can improve photocatalytic efficiency by providing more active sites on the surface [7], [33]. **Figure 4** shows the basic type IV N_2 adsorption-desorption isotherms of BiOCl and BCN-6 with H_3 hysteresis loops, indicating the creation of mesoporous materials during the aggregation and stacking of sheets for BiOCl and BCN-6, respectively [34]. This is entirely consistent with the SEM analysis results above regarding the stacked single-sheet structure of BCN-6. With characteristics of mesoporous materials such as pore width ranging from 2 to 50 nm, significant specific surface areas, and substantial pore volumes. The parameters of total pore volume (V_{pore}), surface area (S_{BET}), and average pore width (W_{pore}) are shown in **Table 1**, in accordance with the theory of mesoporous materials. The surface area of BCN-6 is higher than that of BiOCl, thus it may have higher adsorption and photocatalytic capabilities, which will be verified in the experiments in **section 3.3.**

Table 1. *Total pore volume (V_{pore}), average pore width (W_{pore}), and surface area (S_{BET})*

Sample	Total pore volume (V_{pore}, cm^3/g)	Average pore width (W_{pore}, nm)	Surface area (S_{BET}, m^2/g)
BiOCl	0.049	9.24	21.41
BCN-6	0.041	5.55	30.20

3.2. Optical properties

The samples optical properties were examined using a UV-Vis spectrophotometer. UV-Vis DRS was used to measure and analyze the optical absorption of BiOCl, CNb, and BCN-x samples. In **Figure 5a**, the absorption edges of BiOCl, CNb and the BCN-2, BCN-4, BCN-6, and BCN-8 samples are at wavelengths of 439 nm, 480 nm, 450 nm, 444 nm, 452 nm, and 447 nm, respectively. The absorption edges of the BCN-x composite samples are detected to shift towards the visible region, indicating that

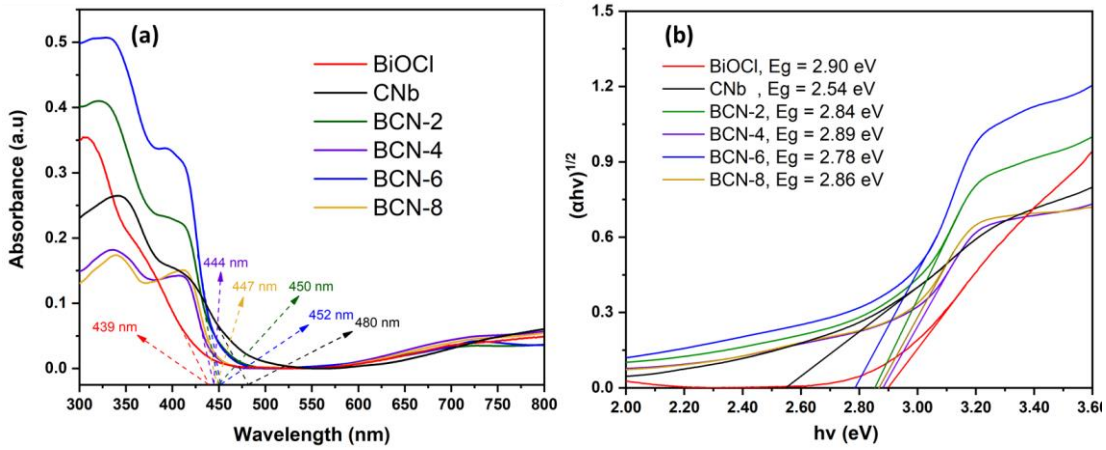

Figure 5. *(a) The DRS UV-Vis spectra and (b) Tauc-plot of CNb, BiOCl and BCN-x.*

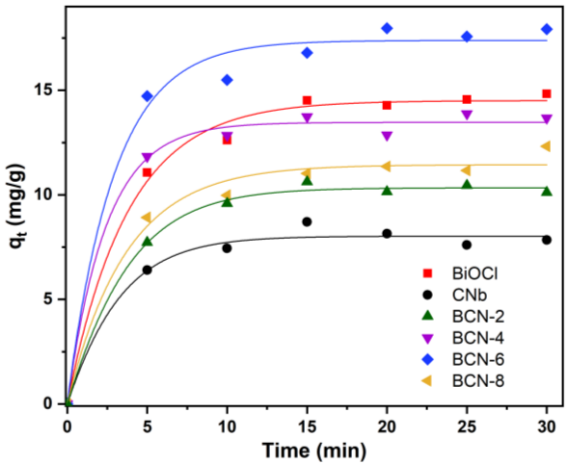

Figure 6. *Adsorption capacity of RhB by CNb, BiOCl, and composite samples over time in dark conditions.*

the presence of CNs on the BiOCl surface extends the light absorption range into the visible region by adding CNs. To calculate the band gap energy of the semiconductor, the following formula can be used:

$$A(hv - E_g)^{\frac{n}{2}} = \alpha hv \quad (2)$$

Where *A*, *h*, *v*, E_g and α are the constant, Planck's constant, light frequency, band gap energy and absorption coefficient, respectively. In this equation, n is defined by the type of band gap energy of the semiconductor ($n = 1$ for direct band gap and $n = 4$ for indirect band gap). Based on earlier reports, the n values for BiOCl and CNb are both 4 [28], [35]. Thus, the E_g of BiOCl and CNb are predicted to be 2.90 eV and 2.54 eV, respectively. **Figure 5b** shows that the E_g values of the BCN-2, BCN-4, and BCN-8 samples did not change significantly as the g-C_3N_4 content increased, ranging from 2.84 to 2.89 eV. It could be seen that either deficiency or excess amount g-C_3N_4 do not lead to the desired band gap results, owing to the coverage level and dispersion of BiOCl on the g-C_3N_4 sheets [36], [37]. However, the BCN-6 sample, with an E_g value of 2.78, shows an improved band gap compared to the other BCN-x samples and a significant improvement compared to the original BiOCl. The conduction band and valence band edge positions of the semiconductor are determined using the following formula:

$$E_{CB} = \chi - E_e - 0.5E_g \quad (3)$$

$$E_{VB} = E_{CB} + E_g \quad (4)$$

Where E_{VB} and E_{CB} are the valence band and conduction band edge positions, X is the absolute electronegativity of the semiconductor (χ = 6.36 and 4.73 for BiOCl and g-C_3N_4, respectively) [38], and E_e is the energy of free electrons on the hydrogen scale (4.5 eV). With the E_g values of BiOCl and g-C_3N_4 being 2.75 and 2.54 eV, respectively, the E_{CB} and E_{VB} values of g-C_3N_4 are determined to be -1.04 and +1.5 eV, respectively, while for BiOCl they are +0.41 and +3.31 eV, respectively. From these numbers, it can be assumed that the VB and CB energy levels of BiOCl and g-C_3N_4 are staggered, forming a structure similar to a type II heterojunction facilitating the effective utilization of electrons and holes generated when exposed to light.

3.3. Photocatalytic activity

$$q_t = \frac{(C_o - C_t).V}{m} \quad (5)$$

$$\frac{t}{q_t} = \frac{1}{q_e}t + \frac{1}{k_{ads}.q_e^2} \quad (6)$$

The following equations are used to estimate the adsorption capacity of pollutants. The adsorption capacities of BiOCl, CNb and BCN-x samples follow the second-order kinetic model [39], and are determined by examining the removal rate of RhB when dissolved in water.

Where: C_O and C_t (mg/L) represent the initial concentration and the concentration at time t of RhB in the solution, respectively, m (g) is the mass of the adsorbent and V (L) is the volume of the solution. q_t (mg/g) is the quantity of RhB adsorbed on the catalyst at time t, k_{ads} (g/mg.min) is the adsorption rate constant, and q_e (mg/g) is the amount of RhB adsorbed on the catalyst at equilibrium.

Figure 6 shows the RhB adsorption capacity of the photocatalysts CNb, BiOCl, and composite samples, which reached a stable state after 30 minutes. The quantity of adsorbed RhB at equilibrium (q_e) is presented in Table 2. The adsorption capacity of the composite samples increased linearly with the percentage of CNs doped into BiOCl, with a tendency to decrease in the BCN-8 sample. This may be owing to the great specific surface area of the oxidized CNs sheets, which, when bonded with BiOCl crystals, increase the surface contact area of the composite samples, thereby enhancing the adsorption capacity. However, in the BCN-8 sample, the excessive amount of CNs may cover part of the BiOCl sheets surface area, reducing the contact surface area and consequently decreasing the adsorption capacity compared to the BCN-6 sample.

Table 2. *Adsorption capacity q_e and adsorption rate constant k_{ads}*

Sample	q_e (mg/g)	k_{ads} (g/mg.min)	R^2 (k_{ads})	k_{app} (min^{-1})	R^2 (k_{app})
BiOCl	14.50	0.0249	0.99	0.0819	0.97
CNb	8.02	0.2767	0.98	0.0134	0.95
BCN-2	10.33	0.0443	0.98	0.0777	0.96
BCN-4	14.83	0.0696	0.99	0.0848	0.96
BCN-6	19.92	0.0287	0.98	0.1132	0.98
BCN-8	13.62	0.0268	0.98	0.0743	0.96

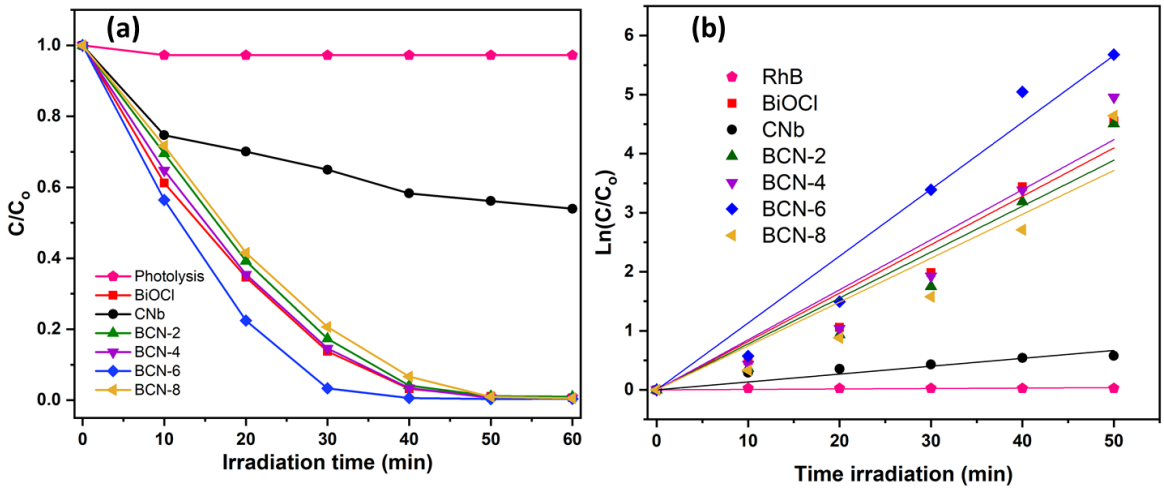

Figure 7. *(a) Rate of RhB degradation under visible light irradiation for the BiOCl, CNb, and BCN-x samples. (b) Kinetics of RhB degradation by the BiOCl, CNb, and BCN-x samples under visible light irradiation.*

To evaluate the photocatalytic efficiency, the research team assessed the degradation capability of the organic dye RhB under visible light irradiation using the BCN-x, BiOCl, and CNb samples **(Figure 7a)**. To determine the stability of RhB under visible light irradiation in water, the experiment was conducted under the same conditions but without any catalyst. The results showed no substantial alteration in RhB concentration, indicating that the self-degradation of RhB could be neglected. For CNb, despite being a semiconductor with a low band gap and visible light absorption, the photocatalytic efficiency of CNb was very poor, reaching only about 50% after 60 minutes of catalysis. This is due to the drawback of g-C_3N_4 with its rapid recombination ability of electrons and holes, thereby inhibiting the reactions from occurring during the photocatalytic process [27]. In contrast, BiOCl still exhibited very good photocatalytic activity, achieving an efficiency of up to 85% after 30 minutes of catalysis. This could be due to the structure of BiOCl in the form of assembled single plates, which increases the contact area between the catalyst and the RhB dye, leading to better RhB degradation. When using

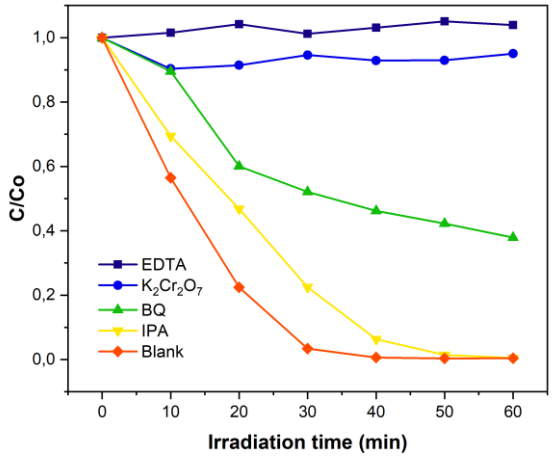

Figure 8. *Trapping experiment of active species for RhB degradation over BCN-6 under visible light irradiation.*

composite samples, the catalytic efficiency was most effectively improved at a concentration of 6% (BCN-6), which could nearly completely degrade RhB dye within just 30 minutes of catalysis. However, adding too many CNs reduces the photocatalytic efficiency, as seen with BCN-8 showing lower photocatalytic performance compared to BCN-6. As mentioned, adding too many CNs can cause the CNs to agglomerate, covering part of the contact area of the BiOCl sheets. This reduces the adsorption capacity and directly affects the photocatalytic efficiency when excessive amount of CNs is used. The kinetics study of the BiOCl, CNb, and BCN-x samples during RhB degradation is shown in **Figure 7b**. The data fits well with the first-order reaction rate model:

$$\ln\frac{C_0}{C_t} = k_{app}.t \qquad (7)$$

Where C_t is the RhB concentration at various irradiation times, C_o is the initial RhB concentration after 30 minutes of adsorption equilibrium, and k_{app} (min^{-1}) is the apparent reaction rate constant. Based on **Table 2** and **Figure 7b**, the K_{app} value for the BCN-6 sample is 0.1132 min^{-1}, which is 8 times and 1.3 times higher than the K_{app} values of CNb (0.0134 min^{-1}) and BiOCl (0.0819 min^{-1}), respectively. The K_{app} values of the BCN-x samples also increase with the CNs ratio, reaching the fastest rate with BCN-6, and then significantly decreasing with BCN-8 when exceeding the optimal CNs amount.

3.4. Catalyst Photostability and Photocatalytic Mechanism

In order to investigate the effects of different reactive species in the photocatalytic process, a series of separate trapping experiments were conducted to capture irradiated electrons (e^-), irradiated holes (h^+), superoxide radicals ($\bullet O_2^-$), and hydroxyl radicals (●OH), various agents such as potassium

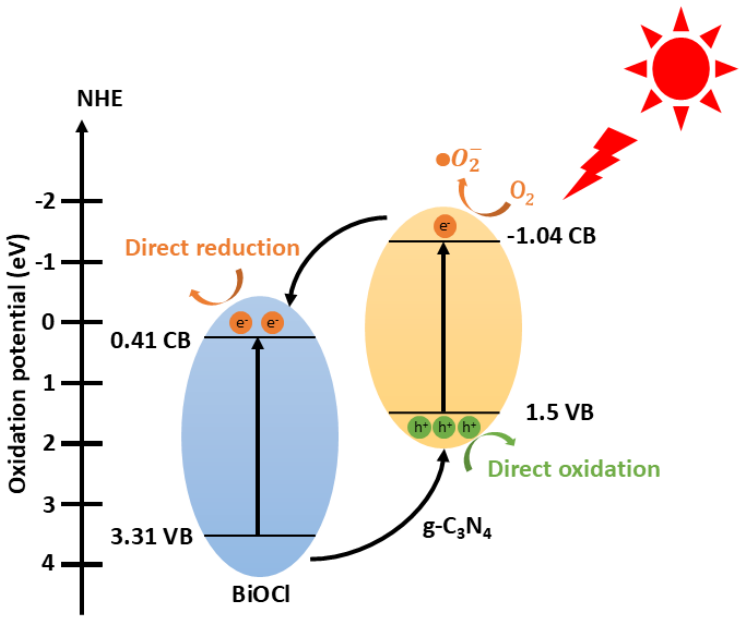

Scheme 1. *Photocatalytic mechanism of g-C_3N_4/BiOCl photocatalysts for the degradation of organic pollutants under visible light radiation.*

dichromate ($K_2Cr_2O_7$), ethylenediaminetetraacetic acid disodium salt (EDTA-2Na), p-benzoquinone (BQ), and isopropanol (IPA) were used, respectively. The concentration of the chelating agents was fixed at 2 mM. As shown in **Figure 8,** the degradation rate of the RhB solution was barely affected when IPA was added, indicating that ●OH radicals play an insignificant role in the oxidation reaction. Meanwhile, when EDTA-2Na and $K_2Cr_2O_7$ were added, the degradation rate significantly decreased, demonstrating that h^+ and e^- are crucial in the redox process of organic pollutants. For BQ, the results showed that $\bullet O_2^-$ has a partial effect, suggesting that few radicals are generated, so it does not significantly impact the degradation rate of organic pollutants.

Based on the results of the reaction species trapping experiments mentioned above, a possible photocatalytic mechanism is illustrated in Scheme 1. When irradiated under visible light, both g-C_3N_4 and BiOCl are excited and generated electron-hole pairs. At this point, excited electrons on the surface of g-C_3N_4 can easily migrate to the CB of BiOCl or partially reduced oxygen in the enviroment to $\bullet O_2^-$ whereas excited holes have tendency to migrate to the VB of g-C_3N_4 without the oxidation reaction (OH^-/●OH) occurred [40]. Since the redox potential ($O_2/\bullet O_2^-$) is lower than CB of g-C_3N_4, reduction is thermodynamically favorable [41]. Thus, remained excited electrons are concentrated in the CB of BiOCl and excited holes are separated in VB of g-C_3N_4. As mentioned above, these electrons and holes would directly react with RhB to degradated products. The reactions continue until totally removed RhB in water within 30 min. The incorporation of g-C_3N_4 with BiOCl has appropriate effect on separating electrons and holes, which can accelerate removal rate 1.4 times and shorten removal times from 50 min (BiOCl) to 30 min (BCN-6).

4. Conclusions

We have successfully synthesized a new and stable g-C_3N_4/BiOCl heterostructure photocatalyst under light. The highest optical activity was achieved at an optimal amount of g-C_3N_4 (x = 6%) combined with BiOCl. Analytical and computational methods confirm that this new heterostructure catalyst has improved the degradation efficiency for RhB dye compared to the single-component photocatalysts g-C_3N_4 and BiOCl. This heterostructure photocatalyst has successfully increased the surface area of the material and overcome the rapid recombination rate between the e^- and h^+ pairs of g-C_3N_4, and reduced the initial bandgap of BiOCl, enabling the photocatalyst material to easily react under visible light conditions for an extended period.

Acknowledgments

This work belongs to the project SV2024-35 funded by the Ho Chi Minh City University of Technology and Education, Vietnam.

Conflict of Interest

The authors declare no conflict of interest.

REFERENCES

[1] J. Yang, J. Hao, S. Xu, J. Dai, Y. Wang, and X. Pang, "Visible-light-driven photocatalytic degradation of 4-CP and the synergistic reduction of Cr (VI) on one-pot synthesized amorphous Nb2O5 nanorods/graphene heterostructured composites," *Chem. Eng. J.*, vol. 353, pp. 100–114, 2018.

[2] H. Kyung, J. Lee, and W. Choi, "Simultaneous and synergistic conversion of dyes and heavy metal ions in aqueous TiO2 suspensions under visible-light illumination," *Environ. Sci. Technol.*, vol. 39, no. 7, pp. 2376–2382, 2005.

[3] Y. Dong *et al.*, "A substrate-free graphene oxide-based micromotor for rapid adsorption of antibiotics," *Nanoscale*, vol. 11, no. 10, pp. 4562–4570, 2019.

[4] I. P. Ozkok, E. U. Cokgor, D. Jonas, and D. Orhon, "Kinetic and microbial response of activated sludge community to acute and chronic exposure to tetracycline," *J. Hazard. Mater.*, vol. 367, pp. 418–426, 2019.

[5] S. Adhikari, S. Selvaraj, and D. H. Kim, "Construction of heterojunction photoelectrode via atomic layer deposition of Fe2O3 on Bi2WO6 for highly efficient photoelectrochemical sensing and degradation of tetracycline," *Appl. Catal. B Environ.*, vol. 244, pp. 11–24, 2019.

[6] M. L. Rache, A. R. García, H. R. Zea, A. M. T. Silva, L. M. Madeira, and J. H. Ramírez, "Azo-dye orange II degradation by the heterogeneous Fenton-like process using a zeolite Y-Fe catalyst—kinetics with a model based on the Fermi's equation," *Appl. Catal. B Environ.*, vol. 146, pp. 192–200, 2014.

[7] X. Zhang *et al.*, "In situ surfactant-free synthesis of ultrathin BiOCl/g-C3N4 nanosheets for enhanced visible-light photodegradation of rhodamine B," *Appl. Surf. Sci.*, vol. 476, pp. 706–715, 2019.

[8] T. T. T. Phan and L. T. Nguyen, "Effect of pH on the photo-Fenton degradation of rhodamine B by Prussian blue/g-C3N4," *Vietnam J. Catal. Adsorpt.*, vol. 12, no. 2, pp. 87–91, 2023.

[9] J. Hou *et al.*, "Narrowing the band gap of BiOCl for the hydroxyl radical generation of photocatalysis under visible light," *ACS Sustain.*

Chem. Eng., vol. 7, no. 19, pp. 16569–16576, 2019.
[10] S. M. Aghdam, M. Haghighi, S. Allahyari, and L. Yosefi, "Precipitation dispersion of various ratios of BiOI/BiOCl nanocomposite over g-C3N4 for promoted visible light nanophotocatalyst used in removal of acid orange 7 from water," *J. Photochem. Photobiol. A Chem.*, vol. 338, pp. 201–212, 2017.
[11] J. Hou *et al.*, "The chemical precipitation synthesis of nanorose-shaped Bi4O5I2 with highly visible light photocatalytic performance," *Mater. Lett.*, vol. 252, pp. 106–109, 2019.
[12] H. Huang, K. Xiao, T. Zhang, F. Dong, and Y. Zhang, "Rational design on 3D hierarchical bismuth oxyiodides via in situ self-template phase transformation and phase-junction construction for optimizing photocatalysis against diverse contaminants," *Appl. Catal. B Environ.*, vol. 203, pp. 879–888, 2017.
[13] H. Cheng, B. Huang, X. Qin, X. Zhang, and Y. Dai, "A controlled anion exchange strategy to synthesize Bi 2 S 3 nanocrystals/BiOCl hybrid architectures with efficient visible light photoactivity," *Chem. Commun.*, vol. 48, no. 1, pp. 97–99, 2012.
[14] J. Hou *et al.*, "Lantern-like bismuth oxyiodide embedded typha-based carbon via in situ self-template and ion exchange–recrystallization for high-performance photocatalysis," *Dalt. Trans.*, vol. 47, no. 19, pp. 6692–6701, 2018.
[15] J. Wen, J. Xie, X. Chen, and X. Li, "A review on g-C3N4-based photocatalysts," *Appl. Surf. Sci.*, vol. 391, pp. 72–123, 2017.
[16] G. Mamba and A. K. Mishra, "Graphitic carbon nitride (g-C3N4) nanocomposites: a new and exciting generation of visible light driven photocatalysts for environmental pollution remediation," *Appl. Catal. B Environ.*, vol. 198, pp. 347–377, 2016.
[17] S. Guo *et al.*, "Phosphorus-doped carbon nitride tubes with a layered micro-nanostructure for enhanced visible-light photocatalytic hydrogen evolution," *Angew. Chemie Int. Ed.*, vol. 55, no. 5, pp. 1830–1834, 2016.
[18] L. Jiang *et al.*, "Doping of graphitic carbon nitride for photocatalysis: a review," *Appl. Catal. B Environ.*, vol. 217, pp. 388–406, 2017.
[19] F. Chang *et al.*, "Construction of exfoliated gC 3 N 4 nanosheets–BiOCl hybrids with enhanced photocatalytic performance," *RSC Adv.*, vol. 4, no. 54, pp. 28519–28528, 2014.
[20] L. Lei, H. Jin, Q. Zhang, J. Xu, D. Gao, and Z. Fu, "A novel enhanced visible-light-driven photocatalyst via hybridization of nanosized BiOCl and graphitic C 3 N 4," *Dalt. Trans.*, vol. 44, no. 2, pp. 795–803, 2015.
[21] S. Shi *et al.*, "Facile preparation of g-C3N4 modified BiOCl hybrid photocatalyst and vital role of frontier orbital energy levels of model compounds in photoactivity enhancement," *J. Colloid Interface Sci.*, vol. 416, pp. 212–219, 2014.
[22] Y. Huang *et al.*, "BiOCl nanoplates decorated on g-C3N4 for enhanced photocatalytic activities," *Int. J. Electrochem. Sci.*, vol. 12, no. 5, pp. 4351–4359, 2017.
[23] L. Song, Y. Pang, Y. Zheng, and L. Ge, "Hydrothermal synthesis of novel gC 3 N 4/BiOCl heterostructure nanodiscs for efficient visible light photodegradation of Rhodamine B," *Appl. Phys. A*, vol. 123, pp. 1–10, 2017.
[24] Y. Bai, P. Q. Wang, J. Y. Liu, and X. J. Liu, "Enhanced photocatalytic performance of direct Z-scheme BiOCl–gC 3 N 4 photocatalysts," *Rsc Adv.*, vol. 4, no. 37, pp. 19456–19461, 2014.
[25] C. Zheng, C. Zhang, G. Zhang, D. Zhao, and Y. Wang, "Enhanced photocatalytic performance of g-C3N4 with BiOCl quantum dots modification," *Mater. Res. Bull.*, vol. 55, pp. 212–215, 2014.
[26] W. Cai, J. Tang, Y. Shi, H. Wang, and X. Jiang, "Improved in Situ Synthesis of Heterostructured 2D/2D BiOCl/g-C3N4 with Enhanced Dye Photodegradation under Visible-Light Illumination," *ACS Omega*, vol. 4, no. 26, pp. 22187–22196, Dec. 2019, doi: 10.1021/acsomega.9b03471.
[27] T. Jia *et al.*, "Ultrathin g-C3N4 nanosheet-modified BiOCl hierarchical flower-like plate heterostructure with enhanced photostability and photocatalytic performance," *Crystals*, vol. 7, no. 9, p. 266, 2017.
[28] F. Al Marzouqi *et al.*, "Controlled microwave-assisted synthesis of the 2D-BiOCl/2D-g-C3N4 heterostructure for the degradation of amine-based pharmaceuticals under solar light illumination," *ACS omega*, vol. 4, no. 3, pp. 4671–4678, 2019.
[29] P. Wilczewska, A. B. Giełdoń, A. F. Borzyszkowska, J. Ryl, T. Klimczuk, and E. M. Siedlecka, "Photocatalytic activity of solvothermal prepared BiOClBr with imidazolium ionic liquids as a halogen sources in cytostatic drugs removal," *J. Photochem. Photobiol. A Chem.*, vol. 382, p. 111932, 2019.
[30] T. Narkbuakaew and P. Sujaridworakun, "Synthesis of tri-s-triazine based gC 3 N 4 photocatalyst for cationic rhodamine B degradation under visible light," *Top. Catal.*, vol. 63, pp. 1086–1096, 2020.
[31] L. Li, M. Zhang, Z. Zhao, B. Sun, and X. Zhang, "Visible/near-IR-light-driven TNFePc/BiOCl organic–inorganic heterostructures with enhanced photocatalytic activity," *Dalt. Trans.*, vol. 45, no. 23, pp. 9497–9505, 2016.
[32] Z. S. Seddigi *et al.*, "Facile synthesis of light harvesting semiconductor bismuth oxychloride nano photo-catalysts for efficient removal of hazardous organic pollutants," *PLoS One*, vol. 12, no. 2, p. e0172218, 2017.
[33] H. Che *et al.*, "Fabrication of Z-scheme Bi3O4Cl/g-C3N4 2D/2D heterojunctions with enhanced interfacial charge separation and photocatalytic degradation various organic pollutants activity," *Appl. Surf. Sci.*, vol. 455, pp. 705–716, 2018.
[34] F. Dong *et al.*, "In situ construction of g-C3N4/g-C3N4 metal-free heterojunction for enhanced visible-light photocatalysis," *ACS Appl. Mater. Interfaces*, vol. 5, no. 21, pp. 11392–11401, 2013.
[35] Q. Wang, W. Wang, L. Zhong, D. Liu, X. Cao, and F. Cui, "Oxygen vacancy-rich 2D/2D BiOCl-g-C3N4 ultrathin heterostructure nanosheets for enhanced visible-light-driven photocatalytic activity in environmental remediation," *Appl. Catal. B Environ.*, vol. 220, pp. 290–302, 2018.
[36] W. J. Ong, L. L. Tan, S. P. Chai, S. T. Yong, and A. R. Mohamed, "Surface charge modification via protonation of graphitic carbon nitride (g-C3N4) for electrostatic self-assembly construction of 2D/2D reduced graphene oxide (rGO)/g-C3N4 nanostructures toward enhanced photocatalytic reduction of carbon dioxide to methane," *Nano Energy*, vol. 13, pp. 757–770, 2015.
[37] Y. O. Ibrahim, A. Hezam, T. F. Qahtan, A. H. A. Aswad, M. A. Gondal, and Q. A. Drmosh, "Laser-assisted synthesis of Z-scheme TiO2/rGO/g-C3N4 nanocomposites for highly enhanced photocatalytic hydrogen evolution," *Appl. Surf. Sci.*, vol. 534, p. 147578, 2020.
[38] L. Song, Y. Zheng, and C. Chen, "Sonication-assisted deposition–precipitation synthesis of graphitic C 3 N 4/BiOCl heterostructured photocatalysts with enhanced rhodamine B photodegradation activity," *J. Mater. Sci. Mater. Electron.*, vol. 28, pp. 15861–15869, 2017.
[39] T. T. Pham and E. W. Shin, "Influence of g-C_3N_4 Precursors in g-C_3N_4/$NiTiO_3$ Composites on Photocatalytic Behavior and the Interconnection between g-C_3N_4 and $NiTiO_3$," *Langmuir*, vol. 34, no. 44, 2018.
[40] L. Ye *et al.*, "BiOI thin film via chemical vapor transport: photocatalytic activity, durability, selectivity and mechanism," *Appl. Catal. B Environ.*, vol. 130, pp. 1–7, 2013.
[41] F. Li *et al.*, "In-situ one-step synthesis of novel BiOCl/Bi24O31Cl10 heterojunctions via self-combustion of ionic liquid with enhanced visible-light photocatalytic activities," *Appl. Catal. B Environ.*, vol. 150, pp. 574–584, 2014.

Nguyen Van Tai received his bachelor's degree in Materials Technology from the Ho Chi Minh City University of Technology and Education, Ho Chi Minh City, Vietnam, in 2024. He interned at the Sai Gon High-Tech Park (SHTP) laboratory and is currently pursuing a master's program at the Vietnamese-German University (VGU), Vietnam. He has research interests in photocatalysis on semiconductor materials.

Email: 20130058@student.hcmute.edu.vn. ORCID: https://orcid.org/0009-0008-0215-3082

Tran Thi Thu Thao received her B.S. in Materials Technology from Ho Chi Minh City University of Technology and Education, Ho Chi Minh City, Vietnam, in 2024. She conducted research at the Materials Technology Laboratory of the same university and interned at Tang Long Pack Co., Ltd., Ho Chi Minh City, Vietnam. Her research interests include photocatalytic chemical reactions, semiconductor-based photocatalysis, and semiconductor-polymer composite materials.

Email: 20130063@student.hcmute.edu.vn. ORCID: https://orcid.org/0009-0003-4961-9285

Pham Thanh Truc received the B.S. from the Ho Chi Minh City University of Technology, Ho Chi Minh City, Vietnam, in 2013, and the M.S-Ph.D. integrated degree from the School of Chemical Engineering, University of Ulsan, Ulsan, South Korea, in 2018. She is currently a Lecturer with the Department of Materials Technology, Ho Chi Minh City University of Technology and Education (HCMUTE), Vietnam. Her research interests include photocatalytic chemical reactions, photocatalysts based on semiconductor materials and composites of semiconductor-polymeric materials. intelligent control, nonlinear control, modern control theories, and their applications in robotics. Email: trucpt@hcmute.edu.vn. ORCID: https://orcid.org/0000-0003-3958-4878